Dalton Transactions

ROYAL SOCIETY OF CHEMISTRY

PAPER

View Article Online
View Journal | View Issue

Cite this: *Dalton Trans.*, 2025, **54**, 15998

Nanoporous $CoSe_2$ polyhedra imbedded graphene as a high-performance sodium-ion battery anode material

Shujie Liu, Haiguang Guo, Bohao Wang, Liang Qiao, Xiaoying Hu * and Junzhi Li *

Received 12th August 2025,
Accepted 11th September 2025

DOI: 10.1039/d5dt01923k

rsc.li/dalton

Sodium-ion batteries (SIBs) have emerged as promising candidates with the virtues of abundant sodium resources and low cost of sodium salts. $CoSe_2$ as an anode material has attracted much attention because of its high theoretical capacity. However, the low conductivity of $CoSe_2$ still severely hinders its application. Herein, we fabricated a graphene-crosslinked $CoSe_2$ polyhedron composite material (CoPG) by utilizing graphene as the conductive framework and MOF-derived $CoSe_2$ as the active component for energy storage. The carbon layer derived from the MOF can effectively inhibit polyselenide dissolution and, in combination with graphene, construct a double-carbon-layer conductive network that facilitates electron transport. As a result, the as-prepared CoPG3 can deliver a high reversible capacity of 565 mAh g^{-1} at 0.05C. After 100 cycles, its capacity remained at 87% at 0.5C. This work provides a new insight into the relationship between the conductivity and performance of electrode materials for SIBs.

Introduction

The lithium-based battery technologies are becoming very mature as a large number of portable electronic devices,[1–4] such as electric automobiles and personal laptops, are indispensable in daily life. Given the abundance of lithium in the Earth's crust, alternative de-inter/intercalation ions should be taken into consideration for the long-term development.[5,6] Sodium-ion batteries (SIBs) have emerged as promising candidates with the virtues of abundant sodium resources and the low costs of sodium salts.[7,8] Unfortunately, the larger radius of the Na ion (0.106 *vs.* 0.076 nm, Li ion) triggers sluggish kinetics and matching issues with anode materials, leading to unsatisfactory capacity and rate capability.[9] Graphite, a well-studied anode material for Li ion batteries,[10,11] merely holds a Na capacity of 0.15 Ah g^{-1}, and unparalleled Na capacities are also discovered in other Li ion battery anode materials.[12–14] Thus, synthesizing appropriate anode materials for Na batteries is of great urgency.[15,16]

$CoSe_2$, as a member of the transition metal chalcogenides (TMCs) family, has attracted much attention as a potential anode material for SIBs because of its high theoretical capacity.[17–19] Compared to Co–O and Co–S bonds, the Co–Se bond is much weaker and is easy to break and rebond, benefiting the conversion mechanism of $CoSe_2$ in SIBs. Nevertheless, the inferior electrical conductivity of $CoSe_2$ triggers a sluggish sodiation/desodiation process and insufficient Na ion transportation.[20,21] In addition, the accompanying serious volume change issue compromises the performance sustainability. Designing a suitable synthesis route for large-scale $CoSe_2$ with enhanced conductivity and cyclability is essential towards commercialization. Morphology regulation is the ideal method to create buffer space.[22] Due to the variety of metal salts and organic linkers, metal–organic frameworks (MOFs) can adequately function as the template and precursor to yield desired porous polyhedrons.[23,24] To further reduce the electrode pulverization, these porous polyhedrons should be evenly distributed on a conductive matrix rather than being made in the paste directly.[25] Therefore, compositing the selected MOF with graphene for selenation is one promising strategy to reach such a purpose because the wrinkles of graphene can prevent the aggregation of an excess of $CoSe_2$ polyhedrons and the excellent conductivity makes graphene a matrix interlinking each $CoSe_2$ polyhedron. In this scenario, the ratio between $CoSe_2$ and the composite graphene, namely the trade-off between conductivity and active sites, is an important factor which has a great influence on the overall performance towards the large-scale production.[26,27]

Herein, a series of nanoporous $CoSe_2$ polyhedrons imbedded graphene (CoPG) materials with different $CoSe_2$/graphene ratios are synthesized to regulate the relationship between conductivity and electrochemical performance. ZIF-67 is chosen as both the structural template and precursor, and is composited with gra-

Key Laboratory of Materials Design and Quantum Simulation, College of Materials Science and Engineering, Changchun University, Changchun 130022, China.
E-mail: huxy@ccu.edu.cn, lijz91@ccu.edu.cn

phene through sonication at weight ratios of 1 : 1, 2 : 1, and 3 : 1 (ZIF-67 : graphene) for the selenization process. The resulting selenized products are designated as CoPG1, CoPG2, and CoPG3, respectively. The *in situ* transformation introduces chemical bonds between the $CoSe_2$ nanoboxes and graphene, which facilitates ion diffusions and electron transfer. Therefore, when the current density is 0.05C, CoPG3 delivers a discharge capacity of 844 mAh g^{-1}, which stabilizes at 565 mAh g^{-1} in subsequent cycles. Moreover, even at 0.5C, the CoPG3 retains 87% of its initial capacity after 100 cycles.

Experimental

Materials preparation

Synthesis of CoPG. ZIF-67 was synthesized using the co-precipitation method. 328 mg of 2-methylimidazole and 249 mg of cobalt nitrate hexahydrate were dissolved in methanol (20 mL). The prepared mixed solution was deposited at 25 °C for 24 h. The purple precipitate was obtained by centrifugation, washed three times with ethanol and dried at 60 °C. The dried ZIF-67 precursor and graphene were thoroughly mixed using ultrasonic treatment. The resulting mixture was then dried and transferred into a tube furnace along with selenium powder, which was positioned upstream in the gas flow direction. The temperature was increased from room temperature to 550 °C at a rate of 5 °C per minute, held at 550 °C for two hours, cooled down naturally and the selenized powder was ground for use. The selenization products obtained at ZIF-67 to graphene mass ratios of 1 : 1, 2 : 1, and 3 : 1 were designated as CoPG1, CoPG2, and CoPG3, respectively.

Characterization. X-ray diffraction (XRD) patterns were collected by using a Bruker D8 diffractometer using Cu Kα radiation (wavelength 0.15406 nm). Measurements were carried out from 20 to 70°. Scanning electron microscopy (SEM) images of the obtained samples and energy dispersive spectrometry (EDS) analysis were obtained using a Hitachi SU-8010. Detailed microstructural characterization was carried out using a transmission electron microscope (TEM, JEM2100F for high resolution TEM images). The Brunauer–Emmett–Teller (BET) surface area was determined using a JW-BK123F instrument and nitrogen was adsorbed using the Barrett–Joyner–Halenda (BJH) method at 77 K. X-ray photoelectron spectroscopy (XPS) was performed with a Thermo ESCALab 250 analyser operating in constant analyser energy mode, recorded using monochromatic Al Kα radiation (1486.6 eV). Infrared spectra (FTIR) were recorded using an IFS-66V/S infrared spectroradiometer.

Electrochemical measurements. The working electrode is made by grinding the active material ($CoSe_2$, CoPG1, CoPG2 and CoPG3), super P and a mixture of carboxymethylcellulose (CMC) (7 : 1.5 : 1.5 by weight) with water as a dispersant. The above slurry was then applied to copper foil and dried in vacuum at 60 °C for 10 h. The average mass loading of the electrodes was approximately 0.8–1.0 mg cm^{-2}. The coin half-cells of type CR2032 for the Na-ion-battery (SIB) were assembled in an argon filled glove box using a sodium foil as counter electrode, a Celgard 2400 microporous polypropylene membrane as separator and an electrolyte of 1 M $NaClO_4$ dissolved in vinyl carbonate (EC), ethyl methyl carbonate (EMC) and dimethyl carbonate (DMC) (1 : 1 : 1 vol%) with 5.0% fluoroethylene carbonate (FEC).

Results and discussion

Nanoporous $CoSe_2$ polyhedrons are derived from the selenization of ZIF-67 at 550 °C in a N_2 atmosphere. ZIF-67/graphene composites are prepared by mixing ZIF-67 and graphene in a vial with 25 mL ethanol with different weight ratios for ultrasonic dispersion. Then CoPG1, CoPG2 and CoPG3 are obtained by selenization of these ZIF-67/graphene composites at 550 °C. Fig. 1A shows the XRD pattern of pure $CoSe_2$. The peaks in the pattern are well matched with a hastite phase $CoSe_2$ (PDF, card no. 53-0449). The crystal system of the compound is orthorhombic, with the X-ray diffraction space group *Pnnm*. The lattice parameters *a*, *b*, and *c* are 4.8485, 5.7282, and 3.63 Å, respectively (Fig. 1B). Purple balls are Co atoms, yellow balls are Se atoms. The XRD patterns of CoPG1, CoPG2 and CoPG3 are shown in Fig. 1C. After compositing with graphene and the subsequent selenization, CoPG1, CoPG2 and CoPG3 display identical sharp peaks, indicating the hastite phase is retained. After compositing with graphene, these porous polyhedrons are observed to be uniformly distributed on the graphene sheet (Fig. 1D–F).

Fig. 2A shows an SEM image of ZIF-67 polyhedrons; ZIF-67 is a type of zeolitic imidazolate framework self-assembled from methylimidazole and cobalt ions. The sizes of these ZIF-67 polyhedrons are about 500–700 nm. After the selenization at 550 °C, ZIF-67 particles conformally transformed to porous polyhedrons with rough surfaces (Fig. 2B), which well preserves the morphology of ZIF-67. The TEM image also confirms the porous structure, and we can see massive pore-structure inside the $CoSe_2$ polyhedron. One of the disadvantages of $CoSe_2$ being the anode material for SIBs is the volume expansion during the charge/discharge cycle. The void space inside the $CoSe_2$ polyhedron can provide a buffer zone to counteract the volume expansion in the sodiation process. Besides the lattice fringes of 0.171, 0.257 and 0.296 nm corresponding to the (031), (111) and (101) planes of $CoSe_2$, the HRTEM image also confirms that the $CoSe_2$ polyhedron is coated by a carbon layer with an ~10 nm thickness. To analyze the element distribution, an EDS experiment was conducted. As we can see in Fig. 2E, Co, Se, C with a small quantity of N element are evenly distributed in the structure.

After compositing with graphene, these porous polyhedrons are observed to be uniformly distributed on the graphene sheet. As the weight ratio of ZIF-67/graphene is increased, the graphene sheet is gradually covered by $CoSe_2$ polyhedrons, thus yielding CoPG1, CoPG2 and CoPG3 (Fig. 1D–F). The Raman spectra of the pure $CoSe_2$ polyhedrons, CoPG1, CoPG2 and CoPG3 are depicted in Fig. 3A, showing three peaks cen-

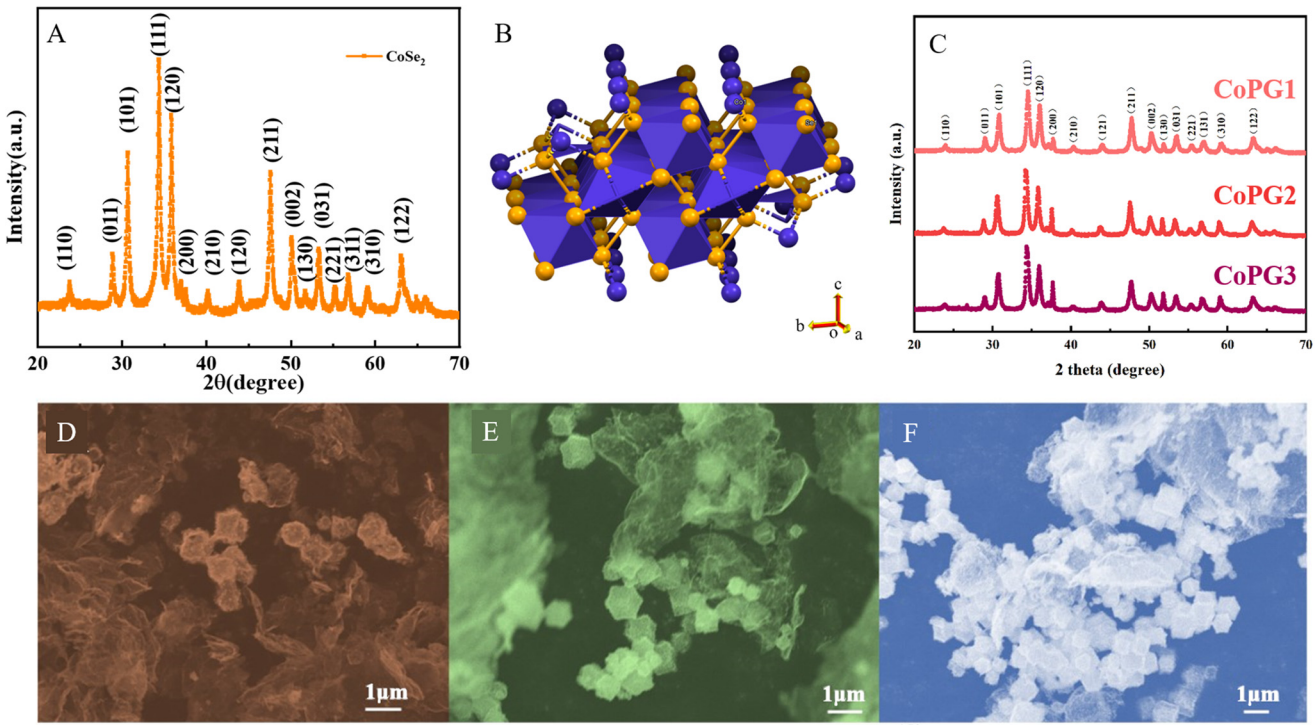

Fig. 1 Phase analysis. (A) The XRD pattern of $CoSe_2$. (B) The crystal structure of the as-prepared $CoSe_2$. Purple balls are Co atoms, yellow balls are Se atoms. (C) The XRD patterns of CoPG1, CoPG2 and CoPG3. Physical characterizations of CoPG1, CoPG2 and CoPG3. (D–F) SEM images of CoPG1, CoPG2 and CoPG3, respectively.

tered around 673, 1350 and 1592 cm^{-1}. The peak located at 673 cm^{-1} is attributed to O7 h spectroscopic symmetry, namely the A_{1g} mode.[28] The other two peaks located at 1350 and 1592 cm^{-1} are the typical D and G bands of carbon materials, caused by the lattice defects and C sp^2 stretching in plane, respectively. As observed in the spectrum of pure $CoSe_2$, the intensities of the D and G bands are inconspicuous implying the amorphous nature of the carbon layer outside the $CoSe_2$ polyhedrons. After compositing with graphene, the D and G bands becomes obvious due to the existence of graphene. As the content increased from CoPG1 to CoPG3, I_D/I_G also increased from 1.02 to 1.22, which evidenced a decreasing graphitization degree. This is because the amount of amorphous carbon is increased, which also indicates a decreased electrical conductivity from CoPG1 to CoPG3. The N_2 adsorption–desorption isotherms of CoPG3 are depicted in Fig. 3B. The CoPG3 sample showed type II nitrogen adsorption–desorption isotherms and H_2 hysteresis loops in the relative pressure (p/p_0) range of 0.5–1.0. The BET surface area of CoPG3 is 96.65 $m^2\ g^{-1}$, and the pore diameter is 14.17 nm. The full XPS survey of the $CoSe_2$ polyhedron is shown in Fig. 3C, in which Se, Co C and N are observed. The typical Se 3d XPS spectrum of the $CoSe_2$ polyhedron shows the binding energies are 55.9 and 54.8 eV for Se $3d_{3/2}$ and $3d_{5/2}$, respectively. And the peak centered around 59.1 eV is attributed to the interaction between Se and C atoms. The XPS spectra of Se 3d for CoPG1 to CoPG3, with the increased graphene content, are shown in Fig. 3D–F for comparison.[21] As shown in Table S1, the CoPG1 to CoPG3 values for the Se $3d_{3/2}$ ratio increased from 23% to 24.7%. The specific area represents another critical factor that significantly influences the overall electrochemical performance of $CoSe_2$.

The electrochemical performances of $CoSe_2$, CoPG1, CoPG2 and CoPG3 as the anode material for SIBs were tested in a 2032-type coin cell with a sodium foil as the counter and reference electrodes. The initial three CV curves for pure $CoSe_2$ ranging from 0 to 3 V at the scan rate of 0.5 mV s^{-1} are shown in Fig. S1. In the following cycles, there are three peaks in the cathodic scan, which is due to the conversion mechanism of $CoSe_2$. There is one prominent peak at 1.95 V with a weak shoulder peak on the left due to formation of $CoSe_2$ from Na_2Se and metallic Co. The conversion mechanism of $CoSe_2$ can be summarized as follows:

Discharge process:

$$CoSe_2 + xNa^+ + xe^- \rightarrow Na_xCoSe_2 \quad (1)$$

$$Na_xCoSe_2 + (2-x)Na^+ + (2-x)e^- \rightarrow CoSe + Na_2Se \quad (2)$$

$$CoSe + 2Na^+ + 2e^- \rightarrow Co + Na_2Se \quad (3)$$

Charge process:

$$Co + 2Na_2Se \rightarrow CoSe_2 + 4Na^+ + 4e^- \quad (4)$$

After compositing with graphene, CoPG1, CoPG2 and CoPG3 all exhibit a sharp peak around 0.8 V caused by the activation process and SEI formation (Fig. S2). In the following cycles, the shape of CV is similar to the pure $CoSe_2$ polyhe-

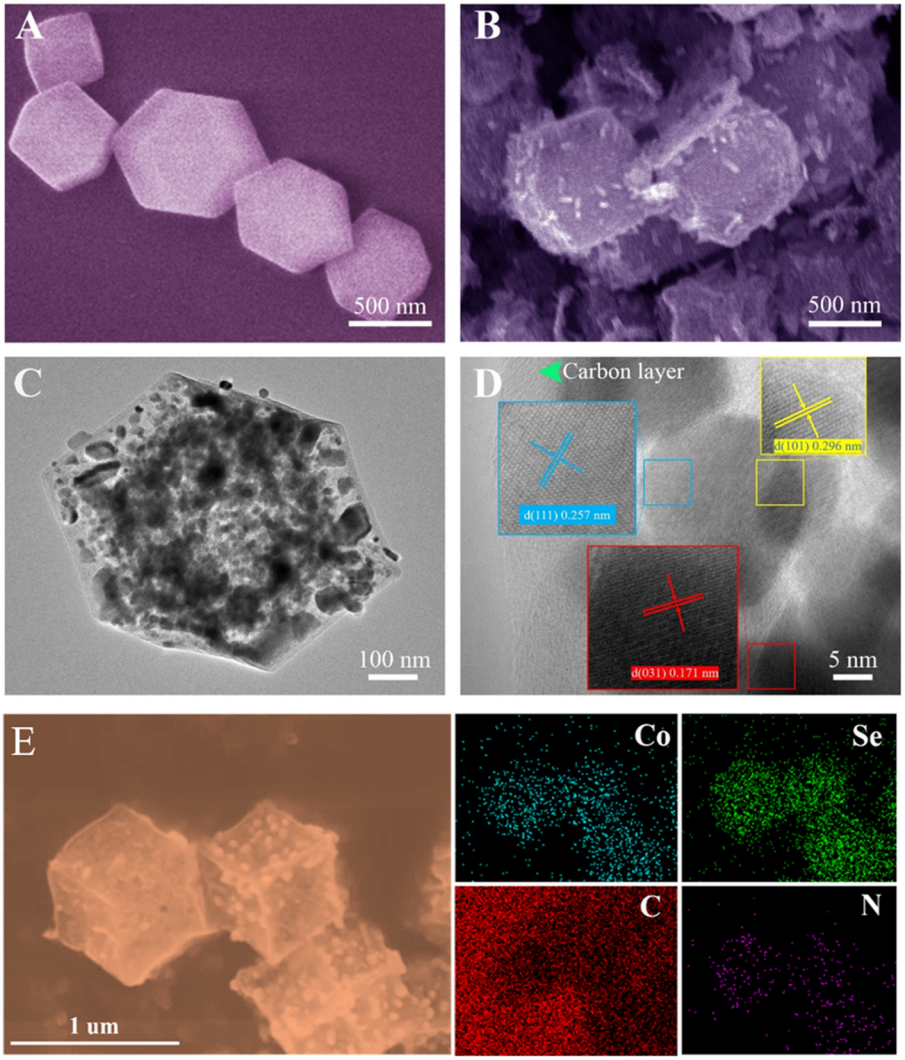

Fig. 2 The morphology characterization from the ZIF-67 polyhedron to nanoporous $CoSe_2$. (A) SEM image of ZIF-67. (B) and (C) SEM and TEM images of nanoporous $CoSe_2$ polyhedrons. (D) HRTEM image of $CoSe_2$ polyhedrons derived from ZIF-67. (E) SEM elemental mapping of $CoSe_2$.

dron, indicating the same conversion mechanism of the composites. Fig. 4A shows the CV comparison of $CoSe_2$, CoPG1, CoPG2 and CoPG3 at the scan rate of 0.5 mV s^{-1}. CoPG3 exhibits the highest peak current among the three composites, and all of them show improved performance compared to the pure $CoSe_2$ polyhedron after incorporating graphene. Correspondingly, the discharge capacity of pure $CoSe_2$ is 572 mAh g^{-1} (0.05C) in the 2nd cycle with an initial coulombic efficiency (CE) of 83.74% (Fig. S3).

Similarly, CoPG1, CoPG2 and CoPG3 all show low CEs in the 2nd cycle (Fig. S4 and Fig. 4B). Fig. 4C shows the charge/discharge profiles in the 3rd cycle for $CoSe_2$, CoPG1, CoPG2 and CoPG3 (0.05C). CoPG3 shows the highest charge capacity of 565 mAh g^{-1}, while the charge capacities of $CoSe_2$, CoPG1 and CoPG2 are 344, 484 and 476 mAh g^{-1}, respectively. The capacities of CoPG1, CoPG2 and CoPG3 are better than $CoSe_2$ due to the introduction of graphene, which greatly enhanced the conductivity of $CoSe_2$. Fig. S5 shows the electrochemical impedance spectroscopy (EIS) measurements, in which we can see that the $CoSe_2$, CoPG1, CoPG2 and CoPG3 charge-transfer resistance R_{ct} decreased from 209.5, 184.9, 70.87 to 55.75Ω and solution resistance changed from 2.13, 4.45, 4.16 to 1.54Ω. The conductive graphene and $CoSe_2$ polyhedrons are interconnected, enhancing both conductivity and active material utilization ratio by alleviating the aggregation phenomenon. As a result, CoPG3 possesses the highest capacity of all. Fig. 4D displays the rate capabilities of $CoSe_2$, CoPG1, CoPG2 and CoPG3. The capacities of CoPG3 are 565, 507, 485, 448, and 376 mAh g^{-1} at 0.05C, 0.2C, 0.5C, 1C and 2C, respectively. Even at 5C, CoPG3 shows a capacity of 154 mAh g^{-1}, holding a 27% retention of the capacity at 0.05C. CoPG1 shows a capacity of 294 mAh g^{-1} at 5C, 60% retention of that at 0.05C. Although inferior at low current rates, CoPG1 exhibits higher capacities than CoPG3 at high current rates, implying the combination of the conductivity and the content of active material should be taken into consideration for appli-

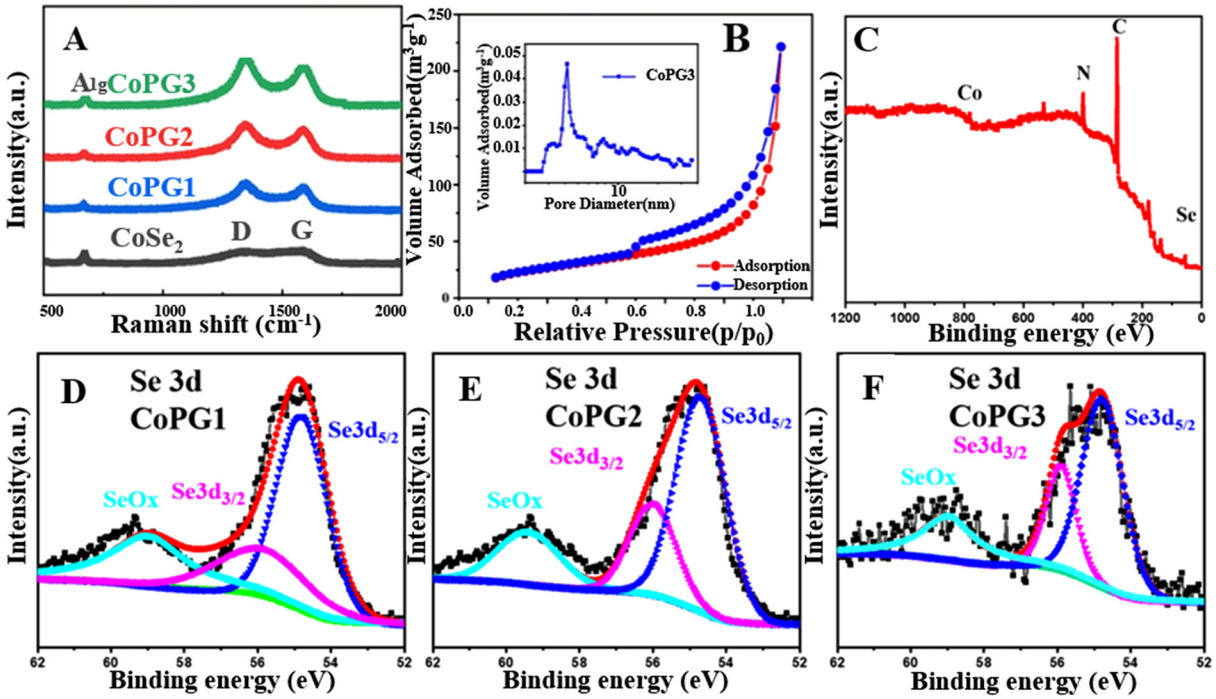

Fig. 3 (A) Raman spectra of $CoSe_2$, CoPG1, CoPG2 and CoPG3. (B) N_2 adsorption–desorption isotherms and pore-size distributions of CoPG3. (C) XPS survey spectra of $CoSe_2$ polyhedron. (D–F). XPS spectra of Se element in CoPG1, CoPG2 and CoPG3, respectively.

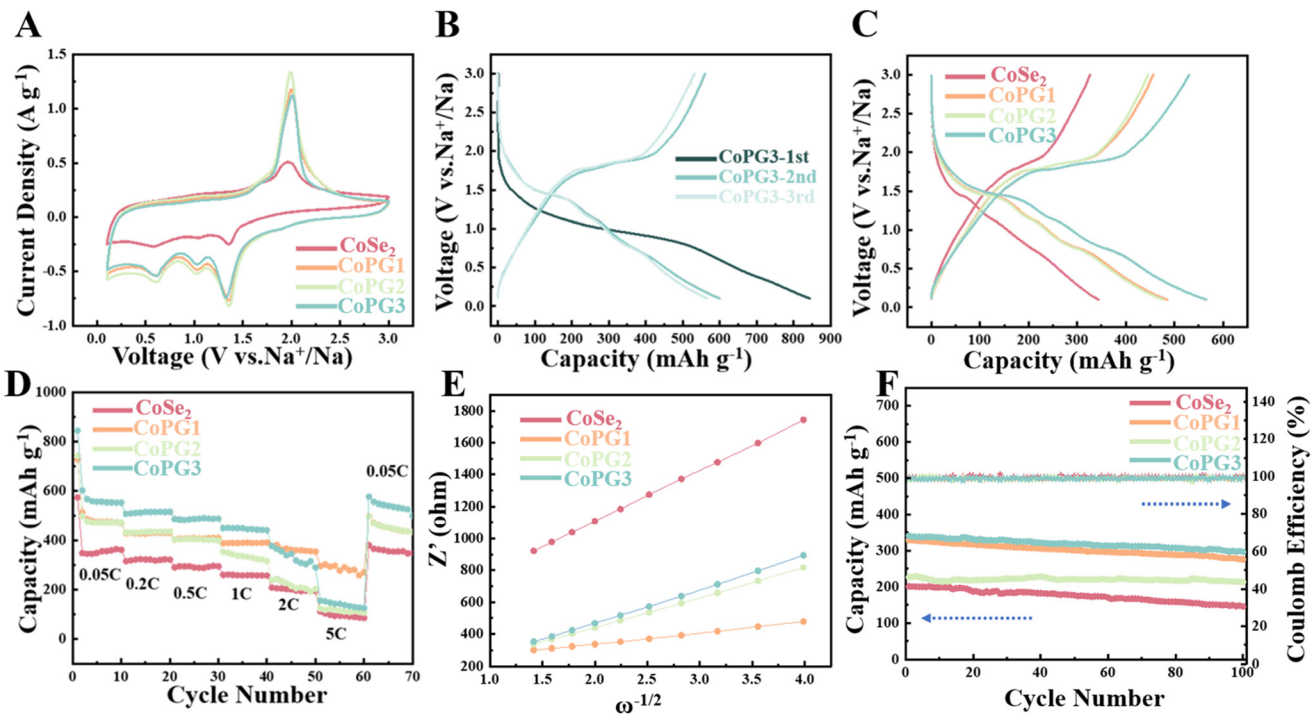

Fig. 4 Electrochemical Na ion storage in $CoSe_2$, CoPG1, CoPG2 and CoPG3. (A) CV curves of $CoSe_2$, CoPG1, CoPG2 and CoPG3. (B) Charge/discharge profiles of CoPG3 (0.05C). (C) Charge/discharge profiles of $CoSe_2$, CoPG1, CoPG2 and CoPG3 (0.05C). (D) Rate performances of $CoSe_2$, CoPG1, CoPG2 and CoPG3. (E) Relationship between Z' and $\omega^{-1/2}$ in the low frequency region of cycled $CoSe_2$, CoPG1, CoPG2 and CoPG3. (F) The cyclability and Coulomb efficiency of $CoSe_2$, CoPG1, CoPG2 and CoPG3 at the current density of 0.5C.

cations. The content of active material is dominant if the goal is to achieve high capacities while the conductivity is much more important in high rate applications. Fig. 4E shows that the slope of CoPG3 is obviously less than that of $CoSe_2$, demonstrating the rapid ion diffusion process. CoPG3 shows a lower slope value than $CoSe_2$ due to the introduction of graphene. As the graphene increases, the slope gradually decreases, implying enhanced Na^+ transport kinetics. Fig. 4F shows the cyclability of $CoSe_2$ CoPG1, CoPG2 and CoPG3 at the current rate of 0.5C. The capacity of CoPG3 remained at 87% after 100 charge and discharge tests, while the Coulomb efficiency remained almost unchanged. To further explore the structural effects of sodium ion intercalation and extraction on CoPG3, we conducted XRD and SEM analyses of CoPG3 following electrochemical reactions. After the electrochemical reaction, the crystallinity of CoPG3 decreased, although the $CoSe_2$ crystal phase was still preserved (Fig. S6a). Fig. S6b presents the SEM image of CoPG3 after the reaction. Although the morphology underwent slight changes, the stable cycling performance demonstrates that these structural alterations do not result in a loss of active sites.

To further investigate the outstanding rate performance of $CoSe_2$ and the graphene composites as the anode material for SIBs, the contributions of capacitive and diffusion-controlled capacities are separated by a series of CV measurements to study the reaction kinetics during the charge/discharge cycle. Fig. S7 and Fig. 5A display 4 similar series of CV curves of $CoSe_2$, CoPG1, CoPG2 and CoPG3 with the scan rate ranging from 0.5 to 3 mV s^{-1}. According to the peak current and scan rate, they obey the following relationship:

$$i = av^b \tag{5}$$

$$\log(i) = b\log(v) + \log(a) \tag{6}$$

where a and b are adjustable parameters. When the value of b approaches 0.5, the diffusion-controlled mechanism is dominant in the charge/discharge cycle. While a value of b approximately equalling to 1, indicates the capacitive behavior is prevailing. The b values of reduction peaks (1, 2 and 3) and oxidation peak (4) of CoPG3 are 0.881, 0.867, 0.850 and 0.764, respectively (Fig. 5B). And the b values of $CoSe_2$, CoPG1 and CoPG2 are summarized in Fig. S8, which all approach to 1

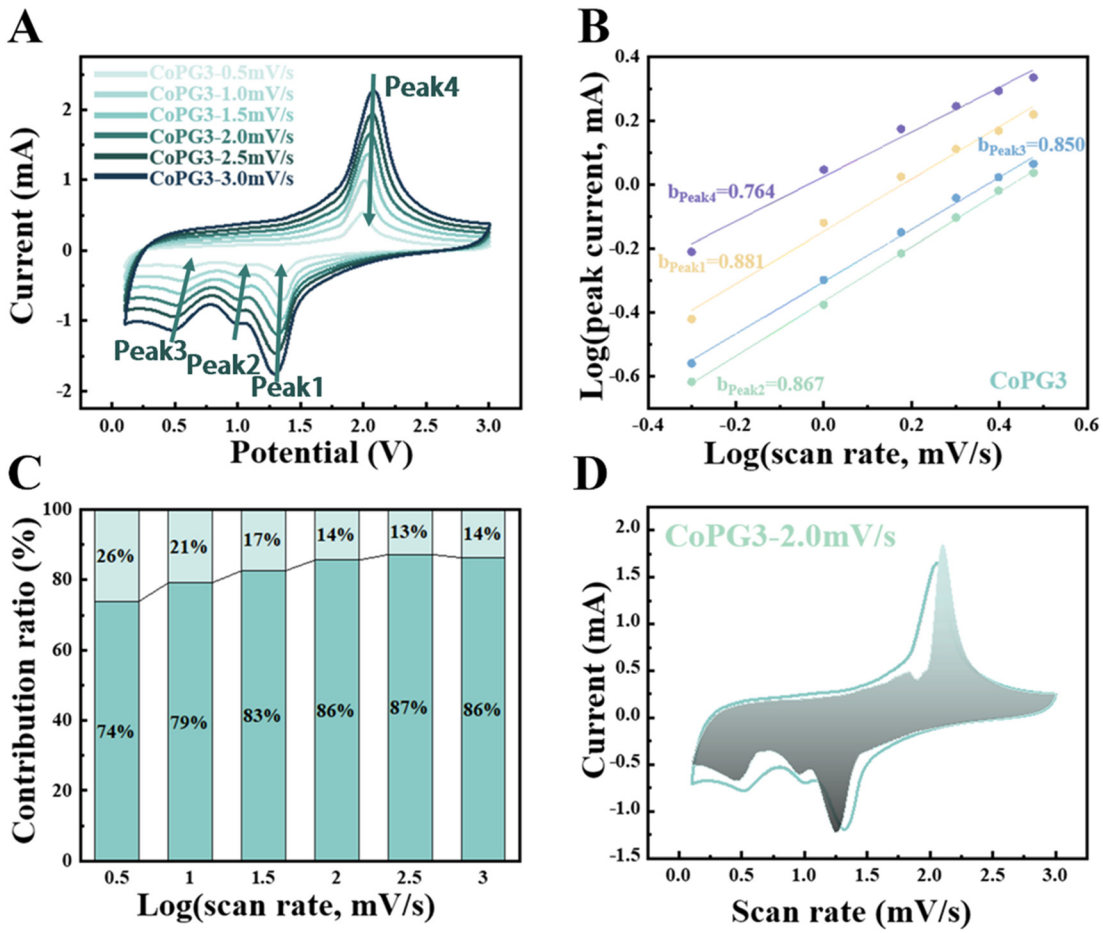

Fig. 5 The kinetics study of CoPG3. (A) The CV curves of CoPG3 at various scan rates. (B) Determination of the b value using the relationship between peak current and scan rate. (C) The contribution of the diffusion-controlled and capacitive capacities from 0.5 to 3 mV s^{-1}. The dark cyan part stands for capacitive contribution, and light cyan part stands for diffusion-controlled capacity. (D) The ratio of capacitive Na ion storage in the total capacity at the scan rate of 2 mV s^{-1}.

indicating the capacitive behavior is dominant. To separate the contributions of capacitive and diffusion-controlled capacities, they can be quantified using the following equation:

$$i = k_1 v + k_2 v^{1/2} \quad (7)$$

where $k_1 v$ and $k_2 v^{1/2}$ are capacitive and diffusion-controlled capacities. As depicted in Fig. 5C, the capacitive contributions of CoPG3 are about 74%, 79%, 83%, 86%, 87% and 86% at the scan rates of 0.5, 1, 1.5, 2, 2.5 and 3 mV s^{-1}, respectively. In addition, Fig. 5D shows the capacitive portion in the total capacity of CoPG3 at the scan rate of 2 mV s^{-1}, which clearly reveals the truth that the capacitive contribution is dominant in the charge/discharge cycle and accounts for the excellent rate capability of CoPG3. Fig. S9 shows the capacitive contributions of $CoSe_2$, CoPG1 and CoPG2. In the comparison we can learn that the introduction of conductive graphene benefits Na^+ ion transfer kinetics during sodiation/desodiation, and also builds a conductive network for high rate electron transfer. As the ratio of $CoSe_2$/graphene is increased, the capacity is increased but the rate capability is lowered. This is because more active sites have anchored on the graphene sheet, so that the capacity is increased. More $CoSe_2$ polyhedrons on the graphene, means more amorphous carbon is present leading to a degraded conductivity of the composites. As a result, the rate capability degrades gradually.

Conclusions

In summary, the CoPG composite material was synthesized using a two-step process, in which $CoSe_2$ was uniformly anchored onto graphene through ultrasonication and subsequent selenization. Benefiting from the incorporation of graphene, the aggregation phenomenon is significantly reduced, thereby enhancing the utilization efficiency of the active material. Moreover, the dual-carbon layer effectively suppresses the dissolution of polyselenides while improving the material's electrical conductivity. The CoPG3 exhibits a high reversible capacity of 565 mAh g^{-1} at a current density of 0.05C. Moreover, it retains 87% of its initial capacity after 100 cycles at 0.5C, demonstrating excellent cycling stability. The ratio between $CoSe_2$ and graphene stands for the trade-off between capacity and rate capability, which provides a new insight into the relationship between the conductivity and performance of electrode materials for SIBs.

Conflicts of interest

There are no conflicts to declare.

Data availability

The data, including figures and tables that support this article, have been included in the supplementary information (SI). Supplementary information is available. These results include CV curves, charge/discharge profiles, EIS, XRD patterns, SEM image. See DOI: https://doi.org/10.1039/d5dt01923k.

Acknowledgements

This research was financially supported by the Science and Technology Development Project of Jilin Province (20240101105JC), Jilin Province Development and Reform Commission (2024C018-9), Department of Human Resources and Social Security of Jilin Province.

References

1 S. Sun, Z. Han, W. Liu, Q. Xia, L. Xue, X. Lei, T. Zhai, D. Su and H. Xia, *Nat. Commun.*, 2023, **14**, 6662.
2 L. Yu, X. He, B. Peng, W. Wang, G. Wan, X. Ma, S. Zeng and G. Zhang, *Matter*, 2023, **6**, 1604–1621.
3 M. Yuan, H. Liu and F. Ran, *Mater. Today*, 2023, **63**, 360–379.
4 W. Li, J. H. Wang, H. Y. Yen and M. Liu, *Adv. Energy Mater.*, 2024, **14**, 2302735.
5 T. F. Yi, T. T. Wei, Y. Li, Y. B. He and Z. B. Wang, *Energy Storage Mater.*, 2020, **26**, 165–197.
6 H. W. Wang, J. Z. Fu, C. Wang, J. Y. Wang, A. K. Yang, C. C. Li, Q. F. Sun, Y. Cui and H. Q. Li, *Energy Environ. Sci.*, 2020, **13**, 848–858.
7 N. Ahmad, L. Yu, M. U. Muzaffar, B. Peng, Z. Tao, S. Khan, A. Rahman, J. Liang, Z. Jiang, X. Ma and G. Zhang, *Adv. Energy Mater.*, 2025, **15**, 2404093.
8 J. Cui, S. S. Yao and J. K. Kim, *Energy Storage Mater.*, 2017, **7**, 64–114.
9 Y. Wang, P. Niu, J. Li, S. Wang and L. Li, *Energy Storage Mater.*, 2021, **34**, 436–460.
10 Z. L. Yu, X. Y. Qu, A. C. Dou, Y. Zhou, M. R. Su and Y. J. Liu, *Ceram. Int.*, 2021, **47**, 1758–1765.
11 G. Li, T. Ouyang, T. Z. Xiong, Z. Jiang, D. Adekoya, Y. Wu, Y. C. Huang and M. S. Balogun, *Carbon*, 2021, **174**, 1–9.
12 E. Goikolea, V. Palomares, S. J. Wang, I. R. de Larramendi, X. Guo, G. X. Wang and T. Rojo, *Adv. Energy Mater.*, 2020, **10**, 2002055.
13 V. Palomares, N. Nieto and T. Rojo, *Curr. Opin. Electrochem.*, 2022, **31**, 100840.
14 E. Gibertini, F. Liberale, C. Dossi, G. Binda, B. Mattioli, R. Bettinetti, A. Maspero, M. Fiore, R. Ruffo and L. Magagnin, *J. Appl. Electrochem.*, 2021, **51**, 1665–1673.
15 Y. Kim, H. Kim, S. Park, I. Seo and Y. Kim, *Electrochim. Acta*, 2016, **191**, 1–7.
16 L. Yu, X. He, B. Peng, F. Wang, N. Ahmad, Y. Shen, X. Ma, Z. Tao, J. Liang, Z. Jiang, Z. Diao, B. He, Y. Xie, B. Qing, C. Wang, Y. Wang and G. Zhang, *Adv. Funct. Mater.*, 2024, **34**, 2406771.
17 J. Yang, H. C. Gao, S. Men, Z. Q. Shi, Z. Lin, X. W. Kang and S. W. Chen, *Adv. Sci.*, 2018, **5**, 1800763.

18 J. J. Ye, X. T. Li, G. Xia, G. H. Gong, Z. Q. Zheng, C. A. Z. Chen and C. Hu, *J. Mater. Sci. Technol.*, 2021, **22**, 100–107.
19 X. Liu, G. B. Xu, T. T. Cheng, L. W. Yang and J. X. Cao, *ChemElectroChem*, 2020, **7**, 846–854.
20 H. Zhou, X. Li, Y. Li, M. Zheng and H. Pang, *Nano–Micro Lett.*, 2019, **11**, 40.
21 S. Liu, S. Sarwar, J. Wang, H. Zhang, T. Li, J. Luo and X. Zhang, *J. Mater. Chem. C*, 2021, **9**, 228–237.
22 H. Tabassum, C. Zhi, T. Hussain, T. Qiu, W. Aftab and R. Zou, *Adv. Energy Mater.*, 2019, **9**, 1901778.
23 B. Y. Guan, X. Y. Yu, H. B. Wu and X. W. Lou, *Adv. Mater.*, 2017, **29**, 1703614.
24 J. Gao, Y. Li, L. Shi, J. Li and G. Zhang, *ACS Appl. Mater. Interfaces*, 2018, **10**, 20635–20642.
25 F. Huang, L. Wang, D. Qin, Z. Xu, M. Jin, Y. Chen, X. Zeng and Z. Dai, *ACS Appl. Mater. Interfaces*, 2022, **14**, 1222–1232.
26 Y. Huang, Z. Wang, Y. Jiang, S. Li, Z. Li, H. Zhang, F. Wu, M. Xie, L. Li and R. Chen, *Nano Energy*, 2018, **53**, 524–535.
27 X. Cheng, D. Li, F. Liu, R. Xu and Y. Yu, *Small Methods*, 2019, **3**, 1800170.
28 H. Li, D. Gao and X. Cheng, *Electrochim. Acta*, 2014, **138**, 232–239.